Nanoscale

COMMUNICATION

View Article Online
View Journal | View Issue

Cite this: *Nanoscale*, 2019, **11**, 19301

Received 7th August 2019,
Accepted 22nd September 2019

DOI: 10.1039/c9nr06760d

rsc.li/nanoscale

Photocatalytic activity of exfoliated graphite–TiO_2 nanoparticle composites

Gloria Guidetti,[a] Eva A. A. Pogna,[b,c] Lucia Lombardi,[d] Flavia Tomarchio,[d] Iryna Polishchuk,[e] Rick R. M. Joosten,[f] Alessandro Ianiro,[f] Giancarlo Soavi,[d,g] Nico A. J. M. Sommerdijk,[f] Heiner Friedrich,[f] Boaz Pokroy,[e] Anna K. Ott,[d] Marco Goisis,[h] Francesco Zerbetto,[a] Giuseppe Falini,[a] Matteo Calvaresi,[a] Andrea C. Ferrari,*[d] Giulio Cerullo*[b] and Marco Montalti*[a]

We investigate the photocatalytic performance of composites prepared in a one-step process by liquid-phase exfoliation of graphite in the presence of TiO_2 nanoparticles (NPs) at atmospheric pressure and in water, without heating or adding any surfactant, and starting from low-cost commercial reagents. These show enhanced photocatalytic activity, degrading up to 40% more pollutants with respect to the starting TiO_2-NPs, in the case of a model dye target, and up to 70% more pollutants in the case of nitrogen oxides. In order to understand the photo-physical mechanisms underlying this enhancement, we investigate the photogeneration of reactive species (trapped holes and electrons) by ultrafast transient absorption spectroscopy. We observe an electron transfer process from TiO_2 to the graphite flakes within the first picoseconds of the relaxation dynamics, which causes the decrease of the charge recombination rate, and increases the efficiency of the reactive species photo-production.

1. Introduction

Air and water pollution are major environmental risks to human health.[1] According to the World Health Organization (WHO),[1] in the last decade one out of every nine deaths was related to air pollution,[2] while at least 1.8 bn people used a contaminated drinking-water source.[3] For air pollution remediation, environmental contaminants[4] (*e.g.* NO, NO_2, SO_2, suspended organic particulate, volatile organic compounds, aromatic hydrocarbons, *etc.*) must be turned into harmless compounds. This can be achieved exploiting photocatalysts to absorb light and produce reactive holes (h) and electrons (e) that degrade the pollutants *via* redox processes.[5] The photocatalytic quantum efficiency (PQE) is defined as the ratio between the rate at which the target molecules undergo photodegradation (moles of molecules per unit time) [mol s^{-1}], and the rate of photon absorption (moles of absorbed photons per unit time) [mol s^{-1}].[6,7] Since photocatalytic degradation relies on the Sun and on the photocatalyst, not consumed during the process,[4,8] this is a potentially low-cost and environment friendly approach for pollution abatement.[4]

Amongst oxide semiconductor photocatalysts[4] (such as ZnO, FeO_3, WO_3), titanium dioxide nanoparticles (TiO_2-NPs) have a wide range of applications, including self-cleaning,[9] sterilization of surfaces,[10] air[11] and water[12] purification. TiO_2-NPs have the advantages of stability in water,[4] biocompatibility[13] and low cost (~1900 USD per ton at 2016 prices [14]). Due to its wide band gap (3.25 eV (ref. 4)), TiO_2 absorbs only the UV part of the solar spectrum.[15] TiO_2-NPs with diameter >10 nm (ref. 7) do not display quantum confinement effects, which would result in a blue shift of the absorption spectra.[6] Hence, TiO_2-NPs exploit just the UV part (~4% [16]) of the solar radiation to perform photodegradation,[4,15,17,18] wasting ~96% of the usable spectrum. Even considering only the UV component, TiO_2-NPs have a modest PQE ~ 10%,[7] limited by the recombination of the photo-generated e–h pairs that occurs with 90% quantum efficiency.[19] The PQE increases with the number of generated e–h pairs per absorbed photon, *i.e.* the photo-generation yield,[19] and with the carriers' lifetime.[7] Integration with materials able to accept e or h may slow down charge recombination, leading to a PQE increase.

The integration of TiO_2 with carbon materials, such as nanotubes,[20] dots,[21] graphene oxide (GO)[22] and reduced gra-

[a]*Department of Chemistry G. Ciamician, Universitá di Bologna, Bologna, 40126, Italy. E-mail: marco.montalti2@unibo.it*
[b]*Department of Physics, Politecnico di Milano, Milano, 20133, Italy*
[c]*NEST, Istituto Nanoscienze-CNR and Scuola Normale Superiore, P. zza S. Silvestro 12, Pisa, 56127, Italy*
[d]*Cambridge Graphene Centre, University of Cambridge, Cambridge CB3 0FA, UK*
[e]*Department of Materials Science and Engineering, Technion Israel Institute of Technology, Haifa, 3200003, Israel*
[f]*Department of Chemical Engineering and Chemistry, Eindhoven University of Technology, Eindhoven, 5612 AZ, Netherlands*
[g]*Institut für Festkörperphysik, Friedrich Schiller Universität Jena, Jena, 07743, Germany*
[h]*Global Product Innovation Department, Italcementi Heidelberg Cement Group, Bergamo, 24126, Italy*

phene oxide (RGO),[23] was pursued to enhance PQE.[22–61] The e–h pair generation and evolution in TiO_2/carbon composites, such as TiO_2/RGO[62,63,61] and TiO_2/graphene quantum dots (GQD),[64] was investigated by transient absorption (TA) spectroscopy.[65] In TiO_2/GQD,[64] TiO_2/RGO[62] and $Ti_{0.91}O_2$/RGO,[63] TiO_2 acts as e acceptor when excited with visible light below the TiO_2 optical gap. In TiO_2/GQD, the e-injection occurs with a time constant <15 fs.[62] In $Ti_{0.91}O_2$/RGO with 0.1 wt% RGO, RGO was found to act as e acceptor, decreasing the recombination rate in TiO_2.[61] Thus, when excited with UV photons above the TiO_2 gap, RGO acts as e-acceptor causing the decrease of the charge carriers' recombination rate, resulting in PQE enhancement. However, ref. 61 did not quantify the lifetime of the photo-generated carriers, because of the limited time resolution used (~μs). Ref. 66 theoretically investigated the charge transfer processes, predicting that charge and energy transfer in TiO_2/single layer graphene (SLG) would proceed in both directions, depending on the energy of the excited charges. Here, we apply ultrafast transient absorption spectroscopy to investigate charge separation in exfoliated graphite/TiO_2. Our results explain the mechanism responsible for the increased PQE in TiO_2/carbon composites.

Our TiO_2/exfoliated graphite (TiO_2/Gr) photocatalyst is prepared by sonication-assisted exfoliation of graphite in presence of TiO_2-NPs, using commercial starting materials suitable for large scale production. Liquid-phase exfoliation (LPE) of graphite typically exploits surfactants,[67,68] such as sodium deoxycholate[69] and pluronics.[70] Here we use the TiO_2-NPs themselves to exfoliate graphite in water and produce the photocatalytic composite. The exfoliation process is investigated varying both sonication time and concentration of TiO_2-NPs and comparing the chemical composition and crystal structure by high-resolution powder X-ray diffraction (HR-PXRD). The photocatalytic activity is evaluated by measuring the rate of degradation of a model organic compound (Rhodamine B) in water under UV irradiation. An increase up to ~40% of the degradation rate, with respect to the TiO_2-NPs used as starting material, is observed.

We also study photodegradation of nitrogen oxides, NO_x. These pollutants are extremely relevant to society since NO_x produced by anthropogenic emissions, in large part by on-road diesel vehicles, are key precursors of fine particulate matter (particle pollution smaller than 2.5 μm) and tropospheric ozone air pollution, that affect human health, crop yields and climate worldwide.[71,72] We find a 70% increase in the photocatalytic activity with respect to TiO_2. The photophysical mechanism underlying this enhanced photocatalytic activity is investigated by ultrafast TA spectroscopy with sub-200 fs time resolution and broad spectral coverage (430–1400 nm). We compare the decays of photo-generated e–h pairs in the composite with those in pristine TiO_2 and we observe that TiO_2-NPs inject e into the graphite flakes. The increased photo-production of reactive species explains the photocatalytic activity improvement, with exfoliated graphite acting as e-acceptor.

2. Results and discussion

The preparation of the photo-catalysts for environmental remediation needs to be as simple as possible, low-cost and easily scalable (*e.g.* photocatalyst in concrete is used up to 3% w/w, hence 70 kg m^{-3}, see ref. 81). As discussed in ref. 82, processes based on hydrothermal synthesis and the use of autoclaves (as, *e.g.*, in ref. 83 and 84) are expensive (because of the cost of the equipment), difficult to control (the morphology and activity of the final product is affected by minimal changes in the process) and hazardous, because of the use of high pressures (>2 atm) and high temperatures (>120 °C). Since these risks are proportional to the scale of production, these methods are not suitable for production of tons of photocatalyst, as required considering that in 2018, 30k tons of TiO_2 NPs were used for photocatalytic applications.[85] More generally, since the photocatalytic process is needed to clean the environment, the production of the catalyst itself has to be environmentally friendly and hazardous reagents and high temperatures or pressures should be avoided. State-of-the-art carbon/TiO_2 photocatalytic materials do not meet these requirements, since: (i) they are prepared in multi-step processes (ref. 83); (ii) at high temperatures (>120 °C) and high pressures (>2 atm), such as in ref. 73, 83 and 84; (iii) with toxic reagents, such as in ref. 73; (iv) they cannot be prepared on the multi-ton scale, such as in ref. 73, 83 and 84.

Here we use a one-pot process exploiting sono-chemical reactions at room temperature and atmospheric pressure. This is not disturbed by oxygen and can be scaled up. The process starts from low-cost (~1900 USD per ton at 2016 prices for TiO_2 NPs[14] and ~1000 USD per ton for graphite platelets at 2018 prices[86]) safe reactants, such as graphite and pre-formed TiO_2 NPs, combining all the characteristics required for environmental remediation.

The composites are prepared by ultra sonication of graphite in a 2 mg ml^{-1} aqueous dispersion of TiO_2-NPs for 4 hours (ELMATransonicT460/H-35 kHz) at 40 °C. The exfoliation is performed in Millipore ultrapure water (resistivity 18.2 MΩ cm at 25 °C). We use flakes from Sigma-Aldrich with size ~150 μm and TiO_2-NPs in the anatase form from HOMBIKAT AHP 200, Sachtleben Chemie GmbH (purity of the crystalline phase ≥94% w/w, average surface area ~193 m^2 g^{-1}). Two sets of samples are prepared starting from a different mass ratio of TiO_2 NPs and graphite. Samples having a mass ratio 1 : 1 of TiO_2 with respect to graphite are labelled TiO_2-Gr1:1. Those with a mass ratio 10 : 1 are labelled TiO_2-Gr10:1. TiO_2 NPs are labelled TiO_2.

In order to study the effect of TiO_2-NPs during liquid-phase sonication, we perform HR-PXRD measurements as a function of sonication time. Samples are loaded into 1 mm borosilicate glass capillaries and diffraction patterns collected at ambient temperature with an incident X-ray wavelength of 0.319902 Å. The full width at half maximum (FWHM) of the (002) graphite diffraction peak is deduced by the Rietveld refinement method,[87] using the General Structure Analysis System (GSAS) program and EXPGUI interface.[88,89]

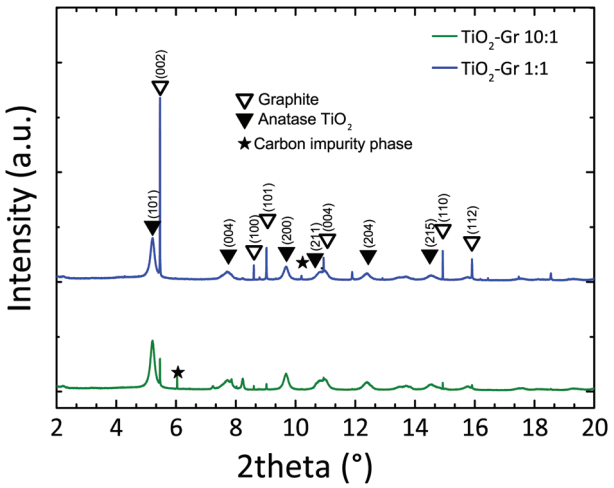

Fig. 1 HR-PXRD diffraction profiles of TiO_2-Gr1:1 and TiO_2-Gr10:1 sonicated for 30 min, with peak assignment.

Diffraction patterns collected after 30 min sonication are shown in Fig. 1. For longer time, up to 4 h, further structural changes are not observed. Thus samples sonicated for 30 min can be considered as the final products. Fig. 1 confirms the presence of TiO_2 anatase (as for The Joint Committee on Powder Diffraction Standards, JCPDS 21-1272[90]) and graphite (JCPDS 75-2078).[91] Moreover, the basal reflection shifts towards higher d-spacings (d_{002} = 3.357 Å) with respect to graphite (JCPDS 75-2078, d_{002} = 3.347 Å (ref. 91)). This suggests that TiO_2-NPs assisted exfoliation increases the interplanar spacing of the resulting flakes. The (002) diffraction peak of TiO_2-Gr10:1 has lower intensity than in TiO_2-Gr1:1. This indicates that an increase in TiO_2-NPs concentration leads to a decrease in the number of planes oriented along (002).[91] As the concentration of TiO_2-NPs increases, the 002 reflection broadens and the corresponding FWHM increases. The broadened FWHM is due to a smaller crystallite size[91,92] (~195 nm, ~241 nm and ~255 nm for TiO_2-Gr10:1, TiO_2-Gr1:1 and graphite, respectively) as determined by the Rietveld method[87] using the software GSAS-II of ref. 93.

We then investigate the photo-physical properties of the samples by UV-visible (UV-Vis) diffuse reflectance spectrometry with a PerkinElmer Lambda45 UV-Vis spectrophotometer with Harricks praying mantis diffuse reflectance. For each sample, 10 mg is mixed with a 500 mg NaCl matrix. We use a quartz cuvette with 0.5 cm optical path. The reflectance background of NaCl (reference) is taken as baseline for each measurement. The diffuse reflectance can be linked to the absorption coefficient through the Kubelka–Munk (KM) function[94] $F(R)$. For a sample thickness >3 mm,[95,96] with no light transmission, $F(R)$ can be written as:[97]

$$F(R) = (1-R)^2/2R = K/s = 2.303\varepsilon \cdot c/s \quad (1)$$

where R is the absolute reflectance, K [cm^{-1}] is the absorption coefficient, s [cm^{-1}] is the scattering coefficient, ε is the

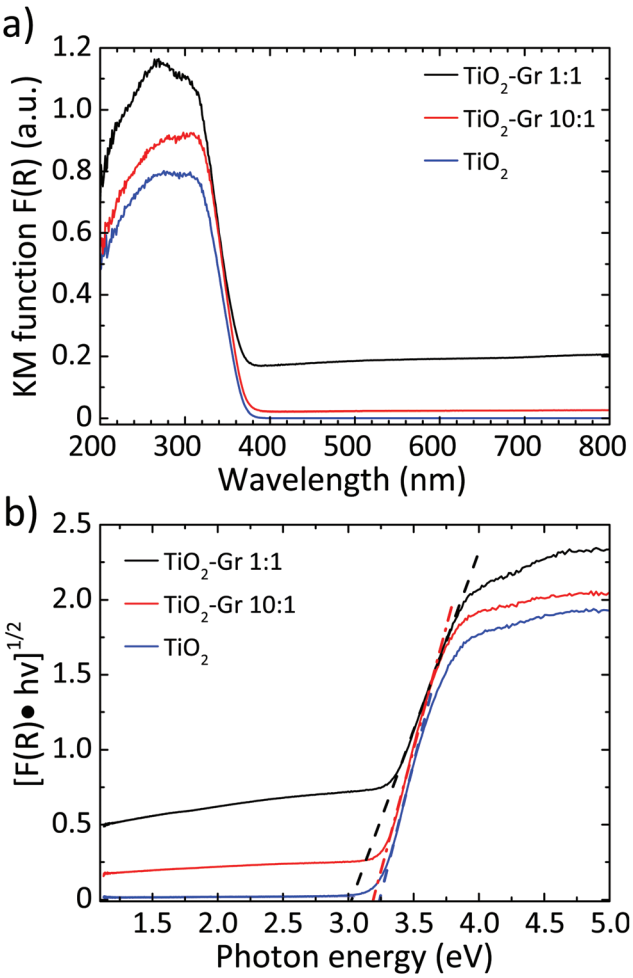

Fig. 2 (a) $F(R)$ elaborated and normalized with KM;[94] (b) Tauc plot of the modified KM function. Dotted lines show the linear extrapolation of the Tauc gap.

absorptivity [mol L^{-1} cm^{-1}] and c is the concentration[M]. Since the samples are dispersed into a non-absorbing matrix (NaCl), s in eqn (1) can be assumed to be that of NaCl and constant.[98] As a consequence, $F(R)$ is proportional to K. Fig. 2a plots the spectra of pristine TiO_2, TiO_2-Gr10:1 and TiO_2-Gr1:1. A transition from the valence to the conduction band of TiO_2 can be seen at ~340–360 nm in all samples, as expected for anatase based composites.[99,100] The presence of exfoliated graphite gives rise to absorption from 400 to 800 nm,[101] and $F(R)$ is higher with respect to pristine TiO_2. An estimation of the band gap can be obtained applying the Tauc equation, which relates absorption edge, energy of incident photons $h\nu$ and Tauc gap E_T:[102]

$$Kh\nu = A(h\nu - E_T)^n \quad (2)$$

where A is a proportionality constant and the index n depends on the interband transitions dominating the absorption. In TiO_2 n = 2 is applied[102] because the interband transitions are indirect. E_T can be determined by a linear extrapolation of

$(F(R)h\nu)^{1/2}$ *versus* $h\nu$, Fig. 2. We get $E_T \sim 3.25$ eV for pristine TiO_2 decreasing to ~3.20 and ~3.02 eV for TiO_2-Gr10:1 and TiO_2-Gr1:1.

The photocatalytic activity is investigated by measuring the photo-degradation of a molecular non-azo-dye (rhodamineB; RhB). This compound is taken as model for organic volatile pollutants, since its molecular structure is close to that of the environmental contaminants used in industry and agriculture.[103] This test follows the same procedures used to characterize other TiO_2–carbon composites.[28,37] TiO_2, TiO_2-Gr10:1 and TiO_2-Gr1:1 are dispersed in an aqueous solution and sonicated for 4 h. In order to understand the effect of the graphite flakes on PQE, the amount of TiO_2-Gr10:1 and TiO_2-Gr1:1 is chosen to guarantee the same concentration of TiO_2 (2 mg ml^{-1}) inside each suspension. We test 10 ml mixtures comprising 2.86%ml of an aqueous solution of RhB (0.05 mg ml^{-1}, 1×10^{-4} M), 2.14% ml H_2O and 50% suspension of TiO_2-Gr10:1 or TiO_2-Gr1:1. Considering the affinity of graphitic flakes, due to the π–π stacking of their aromatic systems, for polycyclic aromatic and cationic compounds like RhB,[104] the suspensions are magnetically stirred for 40 min in the dark, in order to attain adsorption–desorption equilibrium between composite and dye. Ref. 104 reported that, when RhB is adsorbed onto 2–3 layers graphene flakes, there is a ground state interaction that leads to a decrement in the intensity of UV/Vis absorption and photoluminescence (PL) of the dye independent of photodegradation. It is thus necessary to determine the fraction of RhB that remains free inside the solution, since this is required to discriminate whether the change in the dye concentration under irradiation is due to a photoreaction or to adsorption. To obtain the adsorption, after stirring in the dark, 0.75 ml of the RhB-composite suspension is taken and centrifuged at 9000 rpm for 10 min at $T = 25$ °C in order to separate the sample from the RhB solution. The upper 0.5 ml is collected and diluted with water (1 : 6 ratio) to reach the 3 ml volume of analysis of a standard cuvette for a UV/Vis spectrophotometer. The concentration C_D (mol L^{-1}) of free RhB after incubation in the dark is derived from UV/Vis absorption spectra (λ_{max} = 554 nm) recorded at 25° with a Cary300 UV-Vis spectrophotometer and a 180 μm path-length cuvette. The percentage of RhB adsorbed, Ads, is calculated starting from the initial concentration C_0 (mol L^{-1}) of the used dye, as:[105]

$$\text{Ads} = [(C_0 - C_D)/C_0] \times 100 \quad (3)$$

The photoreactivity after photoexcitation of TiO_2 is investigated by exposing each sample to a lamp emitting in the UVA/UVB range (280–400 nm), matching the absorption spectra of the composites, Fig. 2. The lamp has irradiance, *i.e.* emitted power per unit area, $I \sim 3$ W m^{-2} in the UVA (280–315 nm) and ~13.6 W m^{-2} in UVB (315 nm–400 nm), at 0.5 m from the source. The samples are placed 35 cm from the lamp. We use 1 mW UVA/UVB for 60 min, sampling 0.75 ml every time interval t of 10 min. The collected volumes are centrifuged, diluted and analyzed with the same procedure used for the determination of C_D, detecting the concentration $C(t)$ of RhB not degraded after t from the beginning of the irradiation. The percentage of RhB photodegraded, $P(t)$, is:[106]

$$P(t) = [(C_D - C(t))/C_0] \times 100 \quad (4)$$

Using this approach, the photocatalytic activity is assessed independently of the possible adsorption of the dye onto the surface of the photoactive material, since the concentration of the dye after pre-equilibration is taken as a reference. For TiO_2-Gr10:1, Table 1 shows an increment of $P(t)$ with respect to TiO_2 of ~16% after 20 min and ~21% after 40 min. For TiO_2-Gr1:1, the increment is ~7% after 20 min while a decrement ~2% occurs after 40 min. The adsorption of RhB increases from ~5% in TiO_2-Gr10:1 to ~35% in TiO_2-Gr1:1. These results indicate that TiO_2-Gr1:1 does not show improvement in photocatalytic activity with respect to TiO_2. The reason for this is the presence of a residual of graphite that is not electronically interacting with TiO_2 in TiO_2-Gr1:1. The excess of graphite is demonstrated by the broad absorption in the 400–800 nm region in Fig. 2. Graphite adsorbs RhB as demonstrated by the increase of the adsorbed fraction from 5% to 35%, but it is not photocatalyically active. As a result, the fraction of light absorbed by this non-photochemically active component is dissipated without giving photodegradation of RhB, causing a decrease of P. We thus identify TiO_2-Gr10:1 as a promising photocatalytic compound since it gives an enhanced $P(t)$ with respect to TiO_2, for a similar RhB adsorption. The observed lack of improvement in photocathalytic activity of TiO_2-Gr1:1 with respect to TiO_2 is in agreement with ref. 28, 48, 51 and 107, where the adsorption and photocatalytic activity of TiO_2 composites with GO and RGO was reported: a GO/TiO_2 or RGO/TiO_2 weight ratio >10% was associated with a decrease of photocatalytic activity. Hence, we focus on TiO_2-Gr10:1 hereafter.

Fig. 3 compares the concentration of RhB during photodegradation upon UV irradiation for: (i) TiO_2-Gr10:1, (ii) reference TiO_2, (iii) graphite, (iv) no photocatalyst, (v) TiO_2-Gr10:1R which is not ultrasonicated. The trends indicate that the dye's degradation temporal profile is a combination of a zero-order and a first-order kinetics. In zero-order kinetics, the rate is independent of reactant concentration and the RhB concentration decreases linearly with time,[108] while in first order, the rate is proportional to the dye concentration.

Since neither zero-order nor first order models fit the data of Fig. 3, we use a pseudo-zero-order kinetic model commonly

Table 1 Percentage of photodegraded RhB after 20 and 40 min irradiation and adsorption of RhB after incubation in the dark

	TiO_2	TiO_2-Gr10:1	TiO_2-Gr1:1
P(20 min)	38%	54%	45%
P(40 min)	66%	87%	64%
Ads	5%	5%	35%

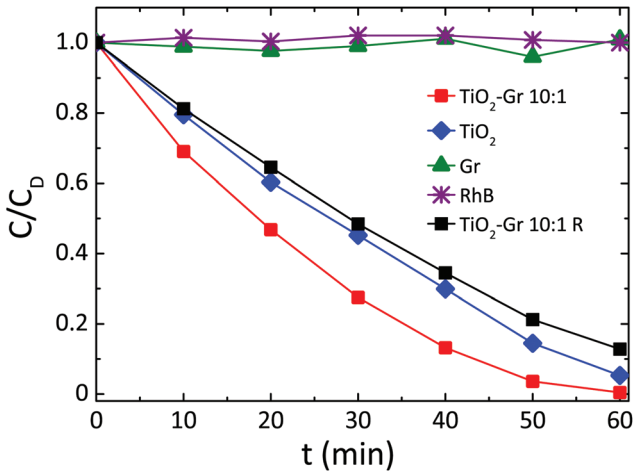

Fig. 3 Photocatalytic degradation of RhB under UV light irradiation in the presence of TiO_2-Gr10:1 ultra-sonicated and not ultra-sonicated (TiO_2-Gr10:1R), TiO_2 and Gr.

adopted in the case of organic dye photodegradation in heterogeneous systems:[109]

$$1 - C(t)/C_D = kt \quad (5)$$

where $k(\text{min}^{-1})$ is the kinetic constant. Fig. 4 fits the data with eqn (5). This gives $k(\text{min}^{-1}) \sim 0.018$ and ~0.025 for TiO_2 and TiO_2-Gr10:1, again indicating that TiO_2-Gr10:1 has higher photoactivity than TiO_2. In order to demonstrate the key role of ultra-sonication in enhancing the photocatalytic activity of TiO_2-Gr10:1, we analyze the photocatalytic degradation of RhB for reference samples, with the same composition but not ultra-sonicated (TiO_2-Gr10:1R). The percentage of photodegraded RhB after 20 minutes $P(20\text{ min})$ is ~36% and after 40 minutes $P(40\text{ min})$ is ~64%, while the fraction of adsorbed RhB after incubation in the dark is ~5%. This performance is similar to that of pristine TiO_2, with no significant improvement, thus demonstrating that ultra-sonication is a key step in order to enhance the photocatalytic performance.

NO_x abatement tests are performed according to the UNI 11247 standard for determination of the degradation of NO_x in air by inorganic photocatalytic materials.[110] (1) An artificial atmosphere generator system with a NO_x source, to provide a continuous flow with a constant NO_x concentration. (2) A reaction chamber containing the sample with a UV lamp (irradiance between 300 and 400 nm, 300 Watt power at 365 nm) providing an accurate light intensity (20 W m^{-2}) on the sample surface. The chamber (3 liters) is sized in order to test samples with a defined exposed surface area (65 cm^2). (3) The NO_x concentration at the outlet is measured with a chemiluminescence NO_x meter, as follows: (1) The sample is placed inside the reaction chamber with the polluted air flow (3 l min^{-1}) and the UV lamp switched off. This phase lasts ~ one hour and is necessary to equalize the adsorption processes and assure a constant NO_x concentration (*i.e.* gas flow stabilization) in the air supply flow. This initial value is noted as C_{OFF}. (2) The UV lamp is switched on and the system is allowed to equalize for a certain time (normally ~ one hour). The irradiated equilibrium concentration is noted as C_{ON}. (3) The UV lamp is switched off and the NO_x concentration is checked to its initial value. The samples are prepared as follows: (i) mixing the composite with 2-propanol, (ii) bath sonication of the mixture for 10 min, (iii) drying at room temperature in a Petri glass to make a thin (1 mm) deposit of the photocatalyst on the bottom of a Petri glass. A fixed incoming flow of air ~1.5 l min^{-1} is used, with a 0.55 ppm concentration of NO_x, including 0.15 ppm NO_2 and 0.4 ppm NO, corresponding to atmospheric pollution as for ref. 111. The NO_x concentrations at the outlet of the reaction chamber measured in stationary flow conditions, either under UV illumination, C_{ON}, or without illumination, C_{OFF}, are shown in Fig. 5 for Gr, TiO_2 and TiO_2-Gr10:1. The NO_x photocatalytic

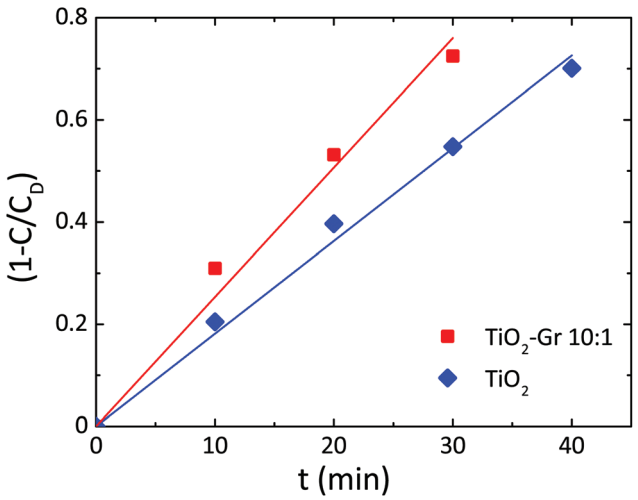

Fig. 4 Photodegradation kinetics of RhB for TiO_2, TiO_2-Gr10:1. Lines are fits to the data with eqn (5).

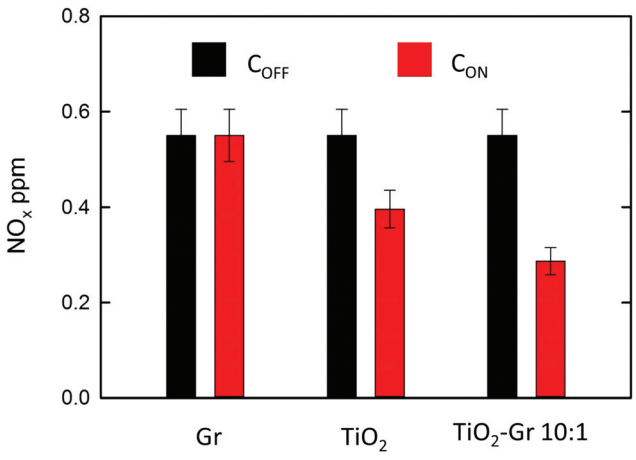

Fig. 5 NO_x concentration measured in stationary flow conditions either under UV illumination (C_{ON}, black bars) or without illumination (C_{OFF}, red bars) at the outlet of the reaction chamber for samples Gr, TiO_2 and Gr-TiO_2 10 : 1.

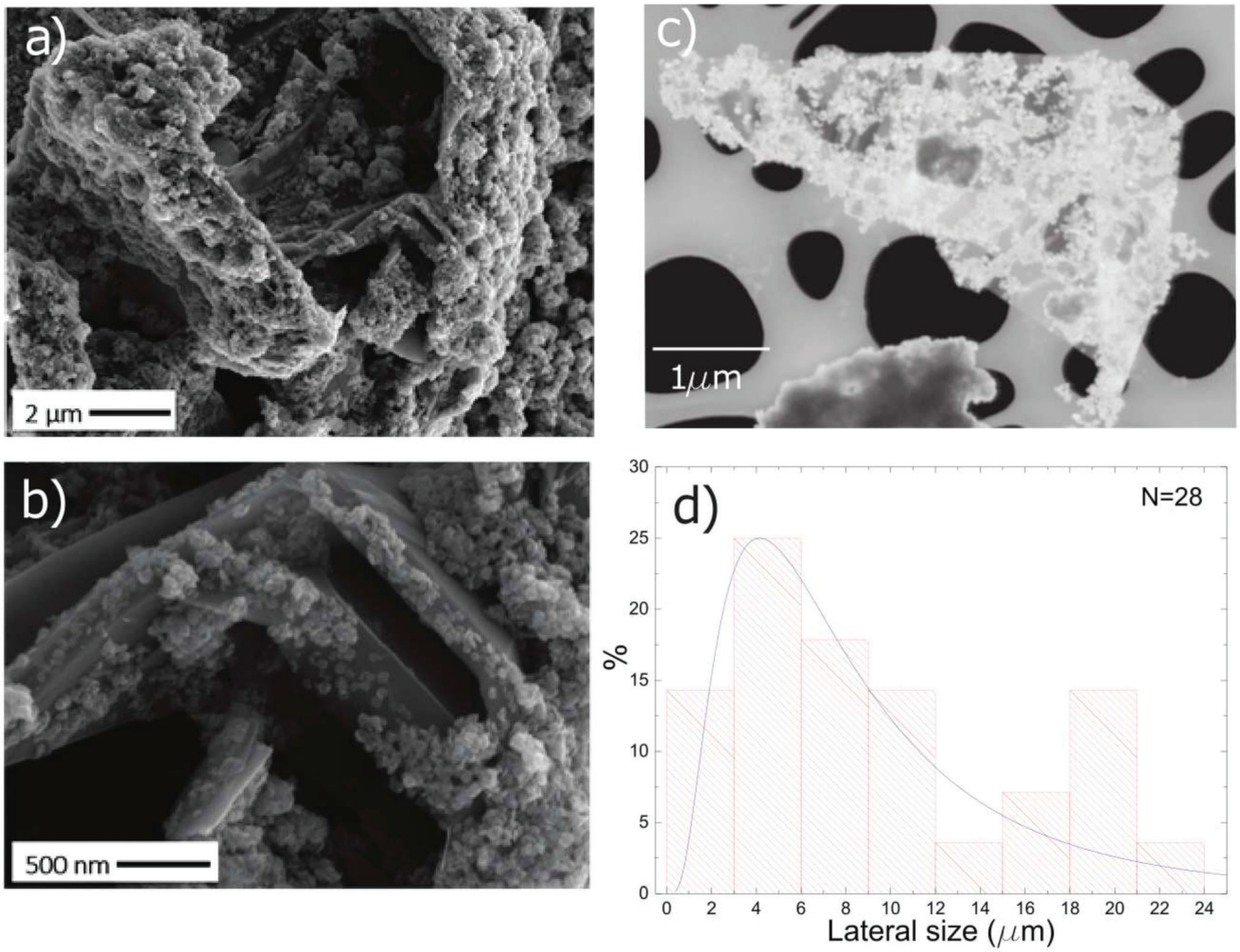

Fig. 6 (a) SEM image of TiO_2-Gr10:1. (b) Higher magnification of (a) showing flakes decorated with NPs. (c) Representative STEM image of a TiO_2-Gr10:1 flake. (d) Distribution of flakes lateral size as determined by STEM of 28 flakes.

decomposition percentage under UV radiation is calculated as $Q = 100(C_{OFF} - C_{ON})/C_{OFF}$. Fig. 5 indicates no NO_x photodegradation for Gr, 28% for TiO_2 and 48% for Gr-TiO_2 10 : 1, with an increase 70% of photodegradation yield of NO_x with respect to TiO_2.

The morphology of TiO_2-Gr10:1 is investigated by scanning electron microscopy (SEM, Quanta3D, FEI Company). Fig. 6a shows graphitic flakes covered by TiO_2-NPs. The higher magnification image Fig. 6b indicates that the flakes edges are decorated by NP agglomerates. The lateral size of the flakes is evaluated by Scanning Transmission Electron Microscopy (STEM, Magellan 400L FEI) depositing ~20 μl TiO_2-Gr10:1 on a holey carbon Cu grid (300 mesh). From a statistical analysis of isolated flakes similar to that in Fig. 6c, an average lateral size ~5 μm is estimated, Fig. 6d.

To exclude that the TiO_2-NPs adhesion to the flakes is due to the drying of the TiO_2-Gr10:1 suspension, we perform Cryo-TEM (CRyoTitan FEI) experiments. 20 μl TiO_2-Gr10:1 is deposited on a holey carbon grid (Quantifoil R2/2 200 mesh), then loaded into the chamber of a FEI Vitrobot™ Mark III, that maintains 100% humidity at 4 °C. Inside the chamber there are two blotting papers on either side of the sample, which close on the grid and leave a layer of suspension ~ hundreds nm thick.[112] The sample is then plunged into liquid ethane at −183.3 °C, which avoids the formation of ice crystals,[113] creating a vitreous ice (amorphous solid form of water).[113] This allows us to investigate themorphology of TiO_2-Gr10:1 in the liquid phase, confirming that TiO_2-NPs adhere to the flakes, both on the surface (red rectangle) and at the edges (blue rectangle), Fig. 7.

TiO_2-Gr10:1 and the starting graphite are also characterized by Raman spectroscopy. 60 μl is drop cast onto a Si/SiO_2 substrate, then heated at 100 °C for 20 min, to ensure water evaporation. Raman spectra are acquired at 514.5 nm using a Renishaw InVia spectrometer with a Leica DM LM microscope and a 50× objective. The power is kept below 1 mW to avoid

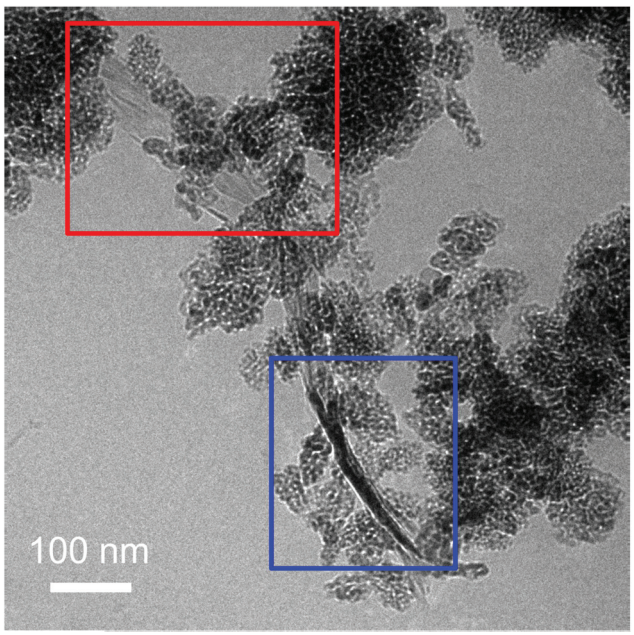

Fig. 7 Cryo-TEM of TiO_2-Gr10:1 in suspension with TiO_2-NPs decorating the flake surface (red rectangle) and the edges (blue rectangle).

any possible damage and heating. The spectral resolution is ~1 cm^{-1}. A statistical analysis is performed as follows: the substrate is divided into 4 regions ~500 × 500 μm^2 and in each 5 points are acquired. Fig. 8 plots representative Raman spectra of the starting graphite (black line) and of TiO_2-Gr10:1 (blue line) both on Si/SiO_2. The peaks at 144, 397, 518 and 639 cm^{-1} are the E_g, B_{1g}, A_{1g} and E_g modes of anatase TiO_2.[114] The TiO_2 peak at 518 cm^{-1} is very close to the first order peak of silicon ~521 cm^{-1} (ref. 115) and they are partially overlapping. The crystallite size of TiO_2-NPs can be estimated from the position Pos(E_g@144 cm^{-1}) and FWHM(E_g@144 cm^{-1}).[116] In our case Pos(E_g@144 cm^{-1}) ~ 147 cm^{-1} and FWHM ~ 20 cm^{-1} correspond to a NPs size ~7 nm,[116] in agreement with an estimate from TEM images, as in Fig. 7, of ~5–10 nm. Fig. 9a and b show no significant difference between Pos(G) and FWHM(G) of graphite and TiO_2-Gr10:1. The 2D peak shape for TiO_2-Gr10:1 still resembles that of graphite[117] with two components ($2D_1$, $2D_2$), but their intensity ratio $I(2D_2)/I(2D_1)$ is reduced from 2.4 to ~1.4, Fig. 9c. This indicates that the bulk flakes have undergone exfoliation.[118]

When compared to the initial graphite, TiO_2-Gr10:1 has a higher $I(D)/I(G)$ and FWHM(G). $I(D)/I(G)$ varies inversely with the crystal size, L_a, according to the Tuinstra and Koenig (TK) relation:[118,119] $I(D)/I(G) \sim 4.4\ nm/L_a$. Alternatively, this can be seen as proportional to the average interdefect distance,[121] L_D: $I(D)/I(G) \sim 130\ nm/L_D^2$. $I(D)/I(G)$ can also be affected by doping.[120] The lack of up shift of Pos(G) and of FWHM(G) narrowing in TiO_2-Gr10:1 when compared to graphite suggests a level of doping similar to the starting graphite, with a negligible effect on $I(D)/I(G)$. We thus derive L_D ~ 31 nm and L_a ~ 33 nm for TiO_2-Gr10:1, and for the starting graphite we get L_D ~ 43 nm and L_a ~ 63 nm. Given the average flakes lateral size in Fig. 7, these numbers reflect the defective nature of the starting graphite, and show that defects increase after sonication. L_a determined by Raman is consist-

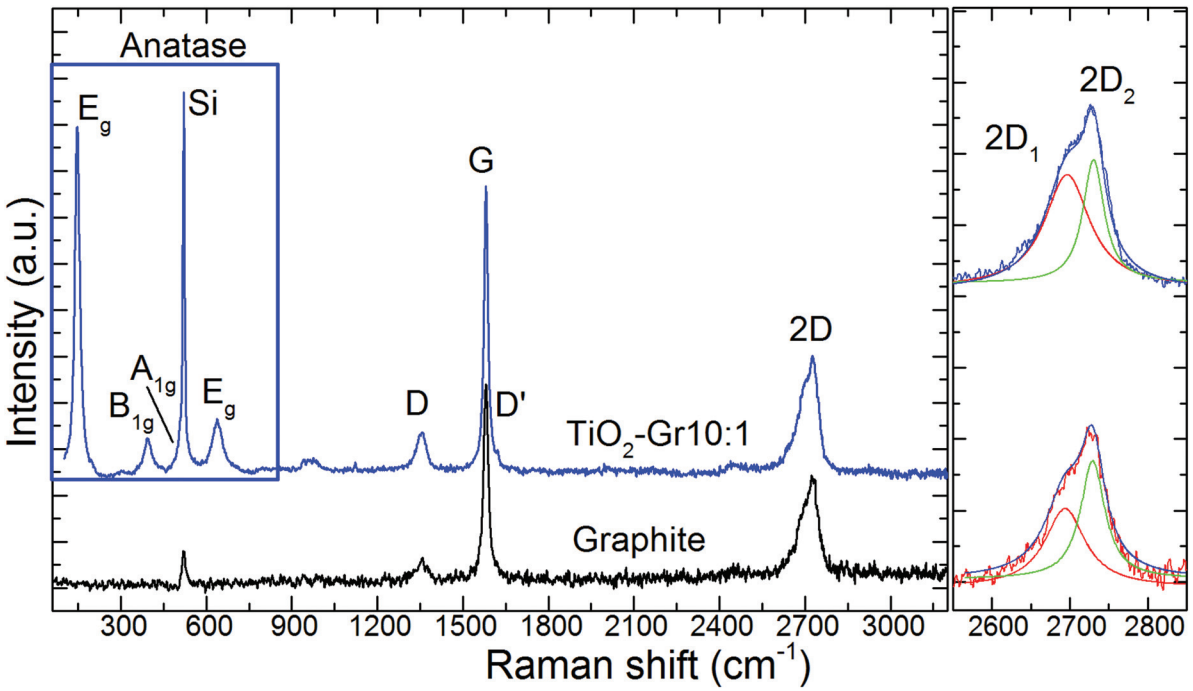

Fig. 8 Representative Raman spectra at 514.5 nm for graphite (black curve) and TiO_2-Gr10:1 (blue curve) both recorded on a Si/SiO_2 substrate.

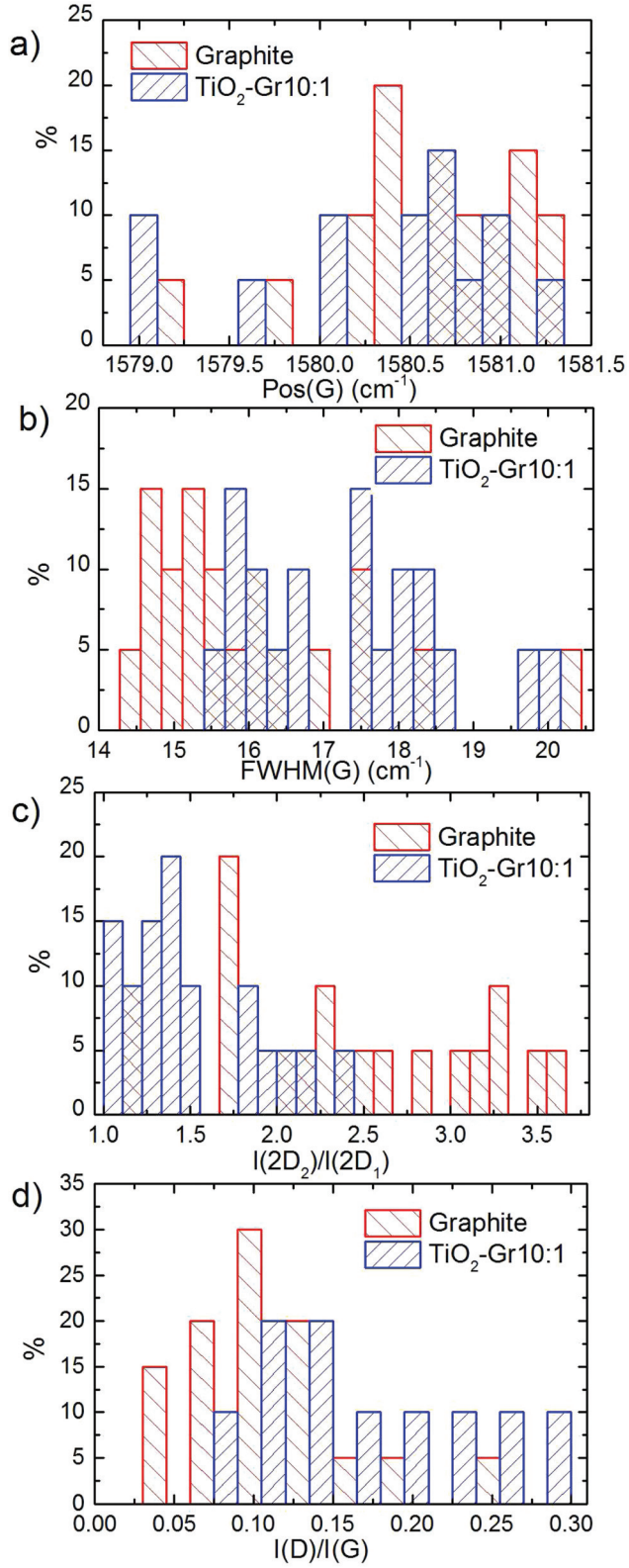

Fig. 9 Distribution of: (a) Pos(G), (b) FWHM(G), (c) $I(2D_2)/I(2D_1)$ and (d) $I(D)/I(G)$.

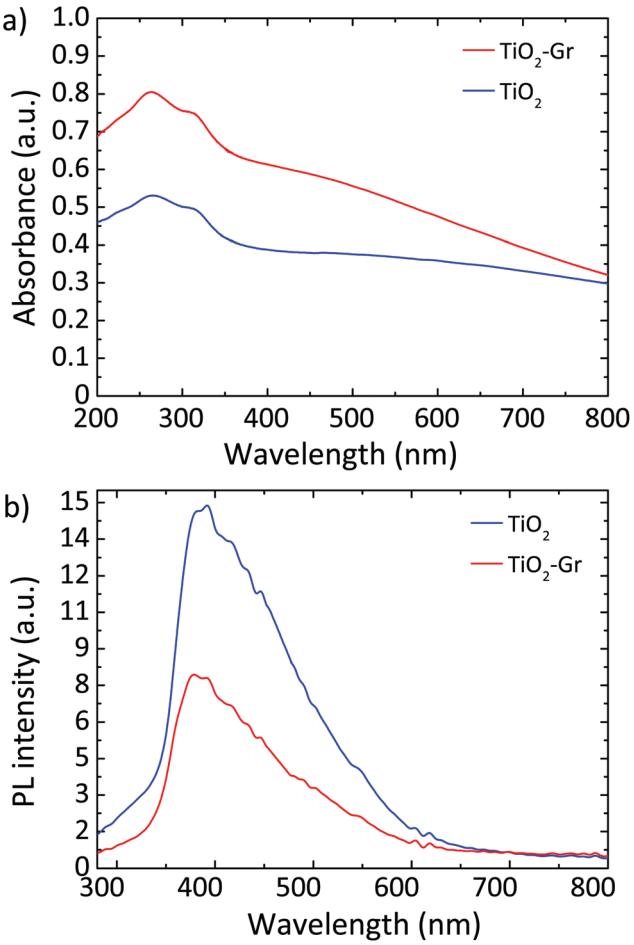

Fig. 10 (a) UV-Vis absorbance of TiO_2 and TiO_2-Gr10:1. (b) PL spectra for 266 nm excitation of TiO_2 and TiO_2-Gr10:1.

ent with that derived from HR-PXRD, although lower. Hence, the Raman spectra in Fig. 8 and their fitting parameters in Fig. 9 indicate that our material has changed with respect to the starting flakes, thus graphite itself is not involved in the photo-catalytic activity.

Fig. 10a plots the UV-Vis absorbance, $-\log_{10}(T)$, with T the transmittance of TiO_2 and TiO_2-Gr10:1. These have two bands in the UV region at 270 and 306 nm, characteristic of TiO_2-NPs,[122] assigned to the first allowed vertical transitions that occur at the center of the Brillouin zone of TiO_2-NPs.[7] The PL spectra of TiO_2 and TiO_2-Gr10:1 in the liquid phase, following excitation at 266 nm, are reported in Fig. 10b. While the shape of the spectra is similar, the PL intensity quenching in TiO_2-Gr10:1 points to an interaction between the excited TiO_2 and the exfoliated graphite, which prevents radiative recombination of the photogenerated e–h pairs.

In order to investigate the photodegradation mechanism, we perform singlet oxygen detection experiments by monitoring the NIR luminescence with an Edinburgh FLS 980 Spectrofluorimeter equipped with a InGaAs detector and a

450 W xenon excitation lamp. Excitation is performed at 350 nm, above the bandgap of TiO_2.[4] No luminescence, hence no singlet oxygen formation, is detected. We thus rule out formation of singlet oxygen during rhodamine photodegradation, in contrast to ref. 123, and suggest that degradation occurs *via* photogeneration of hydroxyl radicals, as for ref. 84.

The generation of reactive oxygen species[5] (ROS) was identified as the photodegradation mechanism of organic pollutants[55] and RhB.[31] The presence of exfoliated graphite in TiO_2-Gr10:1 may result in a higher ROS generation, due to e-transfer from TiO_2 to graphite, allowing a more stable charge separation in TiO_2. The first step of the photocatalytic degradation reaction is the photo-excitation of e–h pairs in TiO_2-NPs by absorption of UV photons with energy exceeding the TiO_2 gap. The ROS generation depends on the competition between charge recombination, either radiative or non-radiative, and the separation of the photo-excited charges required to initiate the oxidative (reductive) pathways.[5] Accordingly, the enhancement of photocatalytic activity may be traced back to modifications of the relaxation channels of photoexcited e–h in TiO_2, induced by graphite flakes.

In order to identify these channels, we perform a comparative study of charge-carriers dynamics in pristine TiO_2 and TiO_2-Gr10:1 using broadband TA spectroscopy with sub-200 fs time-resolution. We use an amplified Ti:sapphire laser (Coherent, Libra) with 100 fs, 500 μJ pulses at 800 nm and 1 kHz. The 266 nm-pump pulse is generated by frequency tripling the laser output and it is modulated with a chopper at 500 Hz. The broadband probe pulse is obtained by white light continuum generation in a plate of sapphire, for the visible, or yttrium aluminium garnet (YAG), for the near-infrared (NIR). The probe spectrum is detected by an optical multichannel analyzer with a wavelength resolution ~1 nm. The parallel linearly polarized pump and probe pulses are focused on the sample in a non-collinear geometry with spot sizes ~180 and ~80 μm, in order to guarantee homogeneous excitation of the detected sample region. The pump power is 1.6 mW, corresponding to an incident fluence ~3 mJ cm^{-2} (~10^{16} photons per cm^2). The measured signal is the delay-dependent differential transmission spectrum,[65] defined as $\Delta T/T(\lambda,\tau) = T_{on}(\lambda,\tau)/T_{off}(\lambda) - 1$, where T_{on} and T_{off} are the probe spectra transmitted through the excited and the unexcited sample, respectively, λ is the probe wavelength and τ the pump–probe delay, controlled with a motorized translation stage. The temporal resolution is ~180 fs. We excite with UV pulses at 266 nm, well above the band gap of TiO_2,[4] and measure $\Delta T/T$ from 430 to 1400 nm.

Fig. 11 plots $\Delta T/T$ (λ,τ) maps as a function of λ and τ. In the NIR, Fig. 11a and b, both TiO_2 and TiO_2-Gr10:1 exhibit broad photo-induced absorption (PA, $\Delta T/T < 0$) from 900 to 1400 nm. We assign it to intraband transitions of the photo-excited free

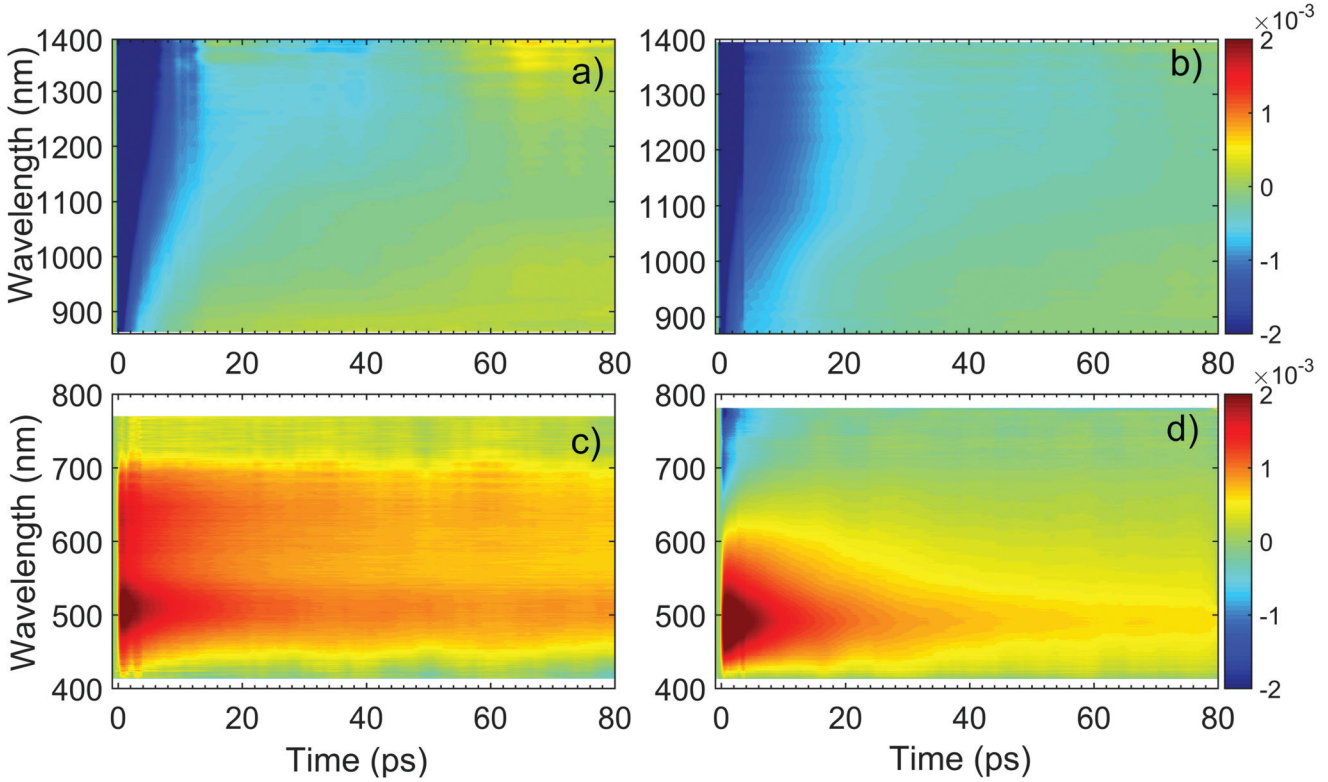

Fig. 11 $\Delta T/T$ maps as a function of probe wavelength and pump–probe delay of TiO_2 in (a) NIR (c) visible. $\Delta T/T$ maps of TiO_2-Gr10:1 in (b) NIR and (d) visible.

e from the conduction band (CB) edge, as reported for anatase TiO_2-NPs.[124–127] An additional source of PA in the NIR comes from the transition of trapped e to the CB.[128] A large variety of trapping states is expected in TiO_2, with energy distribution dependent on sample preparation.[129] According to ref. 125 and 130 the contribution of trapped e to the PA signal should dominate in the range 900–1150 nm, while the free e absorption, which scales as λ^n with n = 1.7,[125] dominates at longer wavelengths. In the NIR, both SLG[131] and multilayer graphene[132] show a positive $\Delta T/T$, corresponding to photo-bleaching (PB) due to Pauli blocking[131,132] from the hot e distribution in the CB.[133,134] Since the TA spectrum of TiO_2-Gr10:1 in the NIR consists of a PA band, we conclude that its optical response is dominated by TiO_2, due both to the higher intensity of the transient signal from TiO_2 and higher concentration of TiO_2 with respect to graphite flakes.

The TA maps of TiO_2-Gr10:1 and TiO_2 in the NIR differ for their time decay, as shown in Fig. 12a. The portion of the PA band in the range 1150–1400 nm can be attributed to free e, as confirmed by the resolution limited formation of the signal in Fig. 12b, and by the monotonic increase of the signal with probe wavelength. For TiO_2, this PA relaxes following a bi-exponential decay with time constants τ_{1TiO_2}/PA = 500 fs, τ_{2TiO_2}/PA = 45 ps. In the presence of exfoliated graphite, the relaxation dynamics is best fit by a three-exponential decay with time constants τ_{1G}/PA = 500 fs, τ_{2G}/PA = 4 ps, τ_{3G}/PA = 20 ps. In both

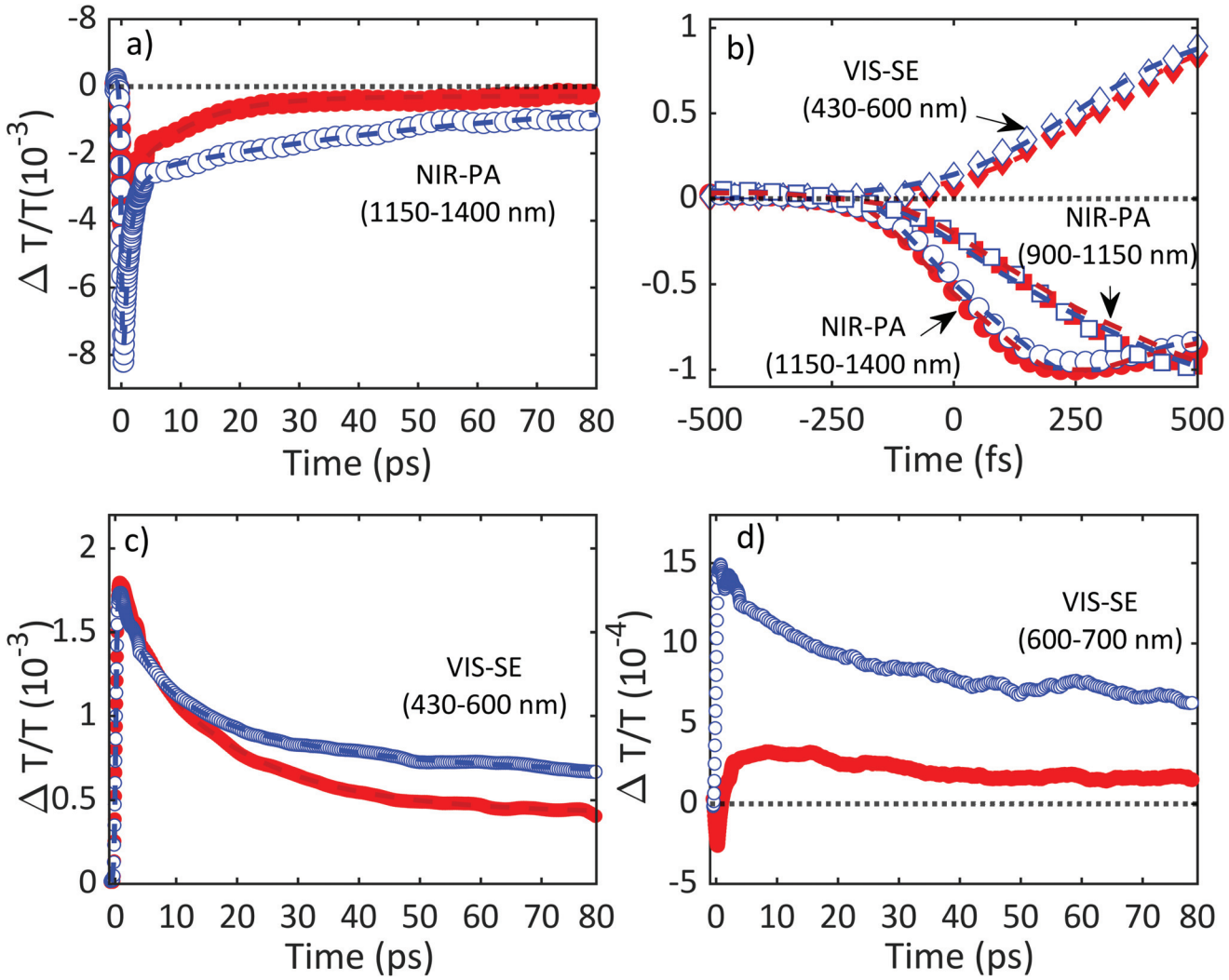

Fig. 12 Relaxation dynamics of TiO_2 and TiO_2-Gr10:1. For all time traces, the empty blue symbols refer to TiO_2 and the filled red ones refer to TiO_2:Gr10:1. (a) NIR-PA in the range 1150–1400 nm together with best fit functions using bi-exponential decay for TiO_2 (blue dashed line) and three-exponential decay for TiO_2-Gr10:1 (red dashed line), both convoluted to the instrumental response. (b) Normalized signal build-up dynamics for TiO_2 and TiO_2-Gr10:1 together with best fit functions. Dashed blue/red lines are fits to the data for TiO_2/TiO_2-Gr10:1 using an exponential build-up convoluted with the instrumental response. The time traces correspond to VIS-SE in the ranges 430–600 nm (diamonds), NIR-PA 1150–1400 nm (circles) and 900–1150 nm (squares). (c) VIS-SE in the range 430–600 nm together with best fits using a biexponential decay function convoluted to the instrumental response (blue/red dashed lines for TiO_2/TiO_2-Gr10:1). (d) VIS-SE dynamics in the range 600–700 nm for TiO_2 (blue open circles) and TiO_2-Gr10:1 (red full circles).

TiO_2 and TiO_2-Gr10:1, the first sub-ps decay component is associated to the trapping of free e.[130,135,136] The appearance of an additional decay channel, and the overall shortening of the PA bands lifetime observed in the composite with respect to the pristine TiO_2-NPs can be explained by ultrafast charge transfer from TiO_2 to the graphite flakes, which act as e scavengers. The PA dynamics in the range 900–1150 nm, mainly related to absorption from trapped e,[125,130] appears almost unperturbed by the presence of exfoliated graphite, suggesting that e transfer mostly involves free e. In both samples, this PA band shows a build-up with a 400–500 fs time constant (Fig. 12b), related to e trapping. This rise time, consistent with the ~200 fs time constant measured in Pt-loaded TiO_2 particles,[137] matches the sub-ps decay component (indicated as τ_{1TiO_2}/PA, τ_{1G}/PA) of PA in the range 1150–1400 nm, observed in both TiO_2 and TiO_2-Gr10:1, which we attribute to free e trapping. Further evidence of e transfer from TiO_2 to flakes can be found in the out-of-equilibrium optical response in the visible range, Fig. 11c and d. In the TiO_2 sample we observe an increase in transmission ($\Delta T/T > 0$) in the visible which, considering the vanishing ground state absorption in this spectral range, can be assigned to stimulated emission (SE), *i.e.* amplification of the probe beam due to optical gain.[65] We identify two overlapping SE bands: the first, in the range 430–600 nm, due to the recombination of free e with trapped h. The second, in the range 600–700 nm, due to recombination of trapped e with free h. In TiO_2-Gr10:1 the second, red shifted SE band is strongly quenched and a residual component appears few ps after excitation, Fig. 12d. The SE band in the range 430–600 nm, related to trapped h recombination can be observed in both samples, but in TiO_2-Gr10:1 it decreases faster to equilibrium, see Fig. 12c. This band has a single exponential build up with 400–500 fs time constant, possibly due to h trapping, Fig. 12b. The SE relaxation dynamics can be fit by a bi-exponential decay on top of a long-lasting component related to the emission on the ns timescale.[127] In TiO_2, we get τ_{1TiO_2}/SE = 5 ps, τ_{2TiO_2}/SE = 45 ps, while in TiO_2-Gr10:1 we have τ_{1G}/SE = 4 ps, τ_{2G}/SE = 20 ps (Fig. 12c). While τ_{1TiO_2}/SE could depend on the lifetime of the trapped h, the other three relaxation components τ_{2TiO_2}/SE, τ_{1G}/SE and τ_{2G}/SE, match those observed for the PA decay in the NIR (equal to τ_{2TiO_2}/PA, τ_{2G}/PA, τ_{3G}/PA) indicating that the SE band at 430–600 nm and the PA band at 1150–1400 nm decay with similar dynamics. These components can be associated to the population dynamics of free e, whose lifetime in TiO_2-Gr10:1 is limited by the charge transfer to graphitic flakes, which occurs on a time-scale ~4–20 ps. Previous ultrafast spectroscopy studies[136,137] on Pt loaded TiO_2-NPs suggested a similar e transfer time of several ps. In our case, e transfer to the graphitic flakes increases the trapped h lifetime, because it inhibits one of their recombination channels, enhancing the oxidative photocatalytic reactivity of the composite.

Fig. 13 summarizes the photoexcitation and relaxation pathways of TiO_2 and TiO_2-Gr10:1 derived from our ultrafast TA experiments. In pristine TiO_2, the free e and h photo-excited into CB and VB by the UV-pump pulse (blue arrow),

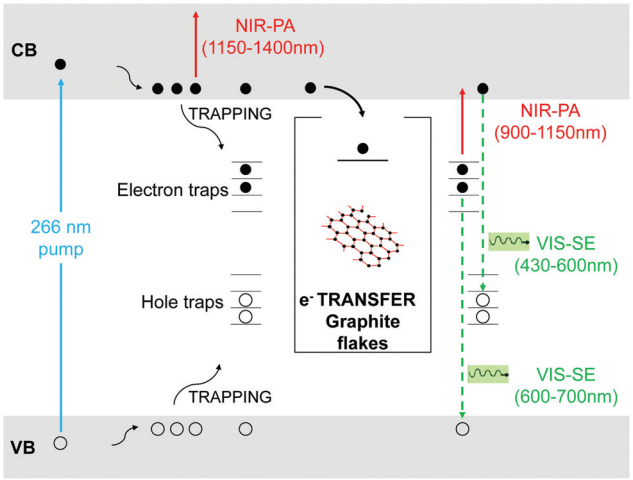

Fig. 13 Schematic illustration of the optical transitions contributing to the TA signals of TiO_2 and TiO_2-Gr10:1. The UV-pump pulse (ciano arrow) photo-excites free-e (full black circles) and -h (empty circles) into CB and VB respectively. Photo-excited charge carriers thermalize to the bands edges and may also get trapped inside-gap states. Photo-excited free-e are monitored by the probe pulse through the PA band in the range 1150–1400 nm (red arrow), and the SE band in the range 430–600 nm (green dashed arrow), related to the recombination with trapped holes. In TiO_2-Gr10:1, free-e can also transfer to graphitic flakes (inset box). The trapped e can radiatively recombine with free h giving rise to the SE band in the range 600–700 nm (green dashed arrow) or be photo-excited into CB as indicated by the PA bands in the range 900–1150 nm.

can either be excited by the probe pulse into higher energy states *via* intraband transitions responsible for the instantaneous PA band in the range 1100–1500 nm, or they can relax into intragap trapped states. The trapped charge carriers can radiatively recombine with free charges giving rise to the SE bands in the range 430–600 nm and 600–700 nm. Trapped e can also be photo-excited into CB as indicated by the PA bands in the range 900–1150 nm. All the bands related to the relaxation of trapped charge carriers share the same build-up dynamics due to the trapping. The interaction with graphitic flakes influences the optical properties of TiO_2-Gr, when compared to TiO_2, by opening an additional relaxation channel for the free e, which can efficiently transfer to the graphite flakes, thus slowing down e–h recombination, enhancing the photocatalytic activity.

3. Conclusions

We reported TiO_2/Gr composites with enhanced photocatalytic activity with respect to pristine TiO_2-NPs. These are produced *via* liquid phase exfoliation of graphite in presence of TiO_2-NPs, without surfactants which could prevent the energy or charge transfer between TiO_2 and graphite flakes. The observed photo-degradation kinetics consists of a combination of zero-order and first-order processes. We assigned the

increase in photocatalytic activity to electron transfer from TiO_2 to the graphite flakes, which occurs within the first ps of the relaxation dynamics.

Our 40% improvement of photocatalytic performance with respect to TiO_2 NPs is almost 400% larger that reported for state of the art RGO-TiO_2.[73] A similar result was achieved in ref. 74, but using carbon nanotubes in combination to RGO. This approach is not suitable for environmental remediation since, due to concerns on toxicity,[75] the dispersion of carbon nanotubes in the environment as a result, *e.g.*, of progressive release from the photocatalytic surfaces, should be avoided. Ref. 76 and 77 showed that water phase exfoliated graphite does not produce environmental concerns. Thus, our composite is designed to fit the requirements for environmental remediation: to treat water (or air) containing pollutants at low concentration (<ppm). Thus, material costs and environmental impact are the main issues. Materials used for environmental remediation, if not properly designed, may become themselves pollutants if dispersed in the environment.[78] It is hence fundamental they are biocompatible. The environmental impact of photocatalyst production also needs to be considered in the assessment of the environmental sustainability of photocatalytic processes for air and water remediation.[79] For different applications, such as fuel photo-production, see *e.g.* ref. 80, different features are required, in particular the value of the photo-product justifies the use of expensive elements such as Pt, Au or Ag.

Due to the simplicity and cost effectiveness of the preparation procedure of our samples, and the enhanced photocatalytic activity in the photodegradation of relevant environmental contaminants such as NO_x, with respect to pristine TiO_2-NPs, we anticipate applications to smart photoactive surfaces for environmental remediation.

Conflicts of interest

There are no conflicts to declare.

Acknowledgements

We thank G. Grancini for useful discussions. We acknowledge funding from the European Union's Horizon 2020 research and innovation programme under grant agreement No. 785219 (GrapheneCore2), EU Neurofibres, ERC Minegrace and Hetero2D, EPSRC Grants EP/509K01711X/1, EP/K017144/1, EP/N010345/1, EP/M507799/5101, and EP/L016087/1.

References

1 http://www.who.int/topics/en.
2 http://www.who.int/mediacentre/news/releases/2016/air-pollution-estimates/en.
3 https://www.unicef.org/publications/files/Progress_on_Drinking_Water_Sanitation_and_Hygiene_2017.pdf.
4 M. R. Hoffmann, S. T. Martin, W. Y. Choi and D. W. Bahnemann, *Chem. Rev.*, 1995, **95**, 69.
5 T. Hirakawa and Y. Nosaka, *Langmuir*, 2002, **18**, 3247.
6 N. Serpone, D. Lawless, R. Khairutdinov and E. Pelizzetti, *J. Phys. Chem.*, 1995, **99**, 16655.
7 N. Serpone, D. Lawless and R. Khairutdinov, *J. Phys. Chem.*, 1995, **99**, 16646.
8 Q. Zhang, Q. An, X. Luan, H. Huang, X. Li, Z. Meng, W. Tong, X. Chen, P. K. Chu and Y. Zhang, *Nanoscale*, 2015, **7**, 14002.
9 Y. Lai, J. Huang, Z. Cui, M. Ge, K. Zhang, Z. Chen and L. Chi, *Small*, 2016, **12**, 2203.
10 S. Nishimoto and B. Bhushan, *RSC Adv.*, 2013, **3**, 671.
11 A. Mamaghani, F. Haghighat and C. S. Lee, *Appl. Catal., B*, 2017, **203**, 247.
12 C. Yu, W. Zhou, H. Liu, Y. Liu and D. D. Dionysiou, *Chem. Eng. J.*, 2016, **287**, 117.
13 T. Xia, M. Kovochich, J. Brant, M. Hotze, J. Sempf, T. Oberley, C. Sioutas, J. I. Yeh, M. R. Wiesner and A. E. Nel, *Nano Lett.*, 2006, **6**, 1794.
14 http://www.cnchemicals.com/Press/88893-CCM.
15 A. L. Linsebigler, G. Q. Lu and J. T. Yates, *Chem. Rev.*, 1995, **95**, 735.
16 I. Foyo-Moreno, I. Alados, F. J. Olmo and L. Alados-Arboledas, *Agric. For. Meteorol.*, 2003, **120**, 101.
17 X. Chen and S. S. Mao, *Chem. Rev.*, 2007, **107**, 2891.
18 A. Fujishima, X. Zhang and D. A. Tryk, *Surf. Sci. Rep.*, 2008, **63**, 515.
19 N. Serpone, *J. Photochem. Photobiol., A*, 1997, **104**, 1.
20 K. Dai, T. Peng, D. Ke and B. Wei, *Nanotechnology*, 2009, **20**, 125603.
21 M. Sun, X. Ma, X. Chen, Y. Sun, X. Cui and Y. Lin, *RSC Adv.*, 2014, **4**, 1120.
22 K. R. Reddy, M. Hassan and V. G. Gomes, *Appl. Catal., A*, 2015, **489**, 1.
23 L. Han, P. Wang and S. Dong, *Nanoscale*, 2012, **4**, 5814.
24 R. Leary and A. Westwood, *Carbon*, 2011, **49**, 741.
25 W. Tu, Y. Zhou and Z. Zou, *Adv. Funct. Mater.*, 2013, **23**, 4996.
26 H. X. Wang, Q. Wang, K. G. Zhou and H. L. Zhang, *Small*, 2013, **9**, 1266.
27 N. Zhang, M. Q. Yang, S. Liu, Y. Sun and Y. J. Xu, *Chem. Rev.*, 2015, **115**, 10307.
28 N. Zhang, Y. Zhang and Y. J. Xu, *Nanoscale*, 2012, **4**, 5792.
29 C. Chen, W. Cai, M. Long, B. Zhou, Y. Wu, D. Wu and Y. Feng, *ACS Nano*, 2010, **4**, 6425.
30 J. Du, X. Lai, N. Yang, J. Zhai, D. Kisailus, F. Su, D. Wang and L. Jiang, *ACS Nano*, 2011, **5**, 590.
31 Y. Gao, X. Pu, D. Zhang, G. Ding, X. Shao and J. Ma, *Carbon*, 2012, **50**, 4093.
32 J. Guo, S. Zhu, Z. Chen, Y. Li, Z. Yu, Q. Liu, J. Li, C. Feng and D. Zhang, *Ultrason. Sonochem.*, 2011, **18**, 1082.
33 B. Jiang, C. Tian, Q. Pan, Z. Jiang, J. Q. Wang, W. Yan and H. Fu, *J. Phys. Chem. C*, 2011, **115**, 23718.
34 C. H. Kim, B. H. Kim and K. S. Yang, *Carbon*, 2012, **50**, 2472.

35 I. Y. Kim, J. M. Lee, T. W. Kim, H. N. Kim, H. I. Kim, W. Choi and S. J. Hwang, *Small*, 2012, **8**, 1038.
36 N. Li, G. Liu, C. Zhen, F. Li, L. Zhang and H. M. Cheng, *Adv. Funct. Mater.*, 2011, **21**, 1717.
37 Y. Liang, H. Wang, H. S. Casalongue, Z. Chen and H. Dai, *Nano Res.*, 2010, **3**, 701.
38 Y. T. Liang, B. K. Vijayan, K. A. Gray and M. C. Hersam, *Nano Lett.*, 2011, **11**, 2865.
39 Y. T. Liang, B. K. Vijayan, O. Lyandres, K. A. Gray and M. C. Hersam, *J. Phys. Chem. Lett.*, 2012, **3**, 1760.
40 J. Liu, Z. Wang, L. Liu and W. Chen, *Phys. Chem. Chem. Phys.*, 2011, **13**, 13216.
41 S. Liu, H. Sun, S. Liu and S. Wang, *Chem. Eng. J.*, 2013, **214**, 298.
42 X. Pan, Y. Zhao, S. Liu, C. L. Korzeniewski, S. Wang and Z. Fan, *ACS Appl. Mater. Interfaces*, 2012, **4**, 3944.
43 L. M. Pastrana-Martinez, S. Morales-Torres, V. Likodimos, J. L. Figueiredo, J. L. Faria, P. Falaras and A. M. T. Silva, *Appl. Catal., B*, 2012, **123**, 241.
44 M. S. A. S. Shah, A. R. Park, K. Zhang, J. H. Park and P. J. Yoo, *ACS Appl. Mater. Interfaces*, 2012, **4**, 3893.
45 J. Shen, M. Shi, B. Yan, H. Ma, N. Li and M. Ye, *Nano Res.*, 2011, **4**, 795.
46 N. P. Thuy-Duong, P. Viet Hung, E. W. Shin, P. Hai-Dinh, S. Kim, J. S. Chung, E. J. Kim and S. H. Hur, *Chem. Eng. J.*, 2011, **170**, 226.
47 P. Wang, J. Wang, T. Ming, X. Wang, H. Yu, J. Yu, Y. Wang and M. Lei, *ACS Appl. Mater. Interfaces*, 2013, **5**, 2924.
48 Y. Wang, R. Shi, J. Lin and Y. Zhu, *Appl. Catal., B*, 2010, **100**, 179.
49 G. Williams, B. Seger and P. V. Kamat, *ACS Nano*, 2008, **2**, 1487.
50 N. Yang, Y. Liu, H. Wen, Z. Tang, H. Zhao, Y. Li and D. Wang, *ACS Nano*, 2013, **7**, 1504.
51 H. Zhang, X. Lv, Y. Li, Y. Wang and J. Li, *ACS Nano*, 2010, **4**, 380.
52 J. Zhang, Z. Xiong and X. S. Zhao, *J. Mater. Chem.*, 2011, **21**, 3634.
53 L. W. Zhang, H. B. Fu and Y. F. Zhu, *Adv. Funct. Mater.*, 2008, **18**, 2180.
54 P. Zhang, C. Shao, Z. Zhang, M. Zhang, J. Mu, Z. Guo and Y. Liu, *Nanoscale*, 2011, **3**, 2943.
55 Y. Zhang, Z. R. Tang, X. Fu and Y. J. Xu, *ACS Nano*, 2010, **4**, 7303.
56 Y. Zhang, Z. R. Tang, X. Fu and Y. J. Xu, *ACS Nano*, 2011, **5**, 7426.
57 Y. Zhang, N. Zhang, Z. R. Tang and Y. J. Xu, *Phys. Chem. Chem. Phys.*, 2012, **14**, 9167.
58 D. Zhao, G. Sheng, C. Chen and X. Wang, *Appl. Catal., B*, 2012, **111**, 303.
59 N. Yang, J. Zhai, D. Wang, Y. Chen and L. Jiang, *ACS Nano*, 2010, **4**, 887.
60 T. F. Yeh, J. Cihlaář, C. Y. Chang, C. Cheng and H. Teng, *Mater. Today*, 2013, **16**, 78.
61 A. Morais, C. Longo, J. R. Araujo, M. Barroso, J. R. Durrant and A. F. Nogueira, *Phys. Chem. Chem. Phys.*, 2016, **18**, 2608.
62 P. Wang, N. M. Dimitrijevic, A. Y. Chang, R. D. Schaller, Y. Liu, T. Rajh and E. A. Rozhkova, *ACS Nano*, 2014, **8**, 7995.
63 K. K. Manga, Y. Zhou, Y. Yan and K. P. Loh, *Adv. Funct. Mater.*, 2009, **19**, 3638.
64 K. J. Williams, C. A. Nelson, X. Yan, L. S. Li and X. Zhu, *ACS Nano*, 2013, **7**, 1388.
65 S. De Silvestri, C. Manzoni, R. Borrego-Varillas, A. Oriana and G. Cerullo, *Riv. Nuovo Cimento*, 2017, **41**, 1.
66 R. Long, N. J. English and O. V. Prezhdo, *J. Am. Chem. Soc.*, 2012, **134**, 14238.
67 Y. Hernandez, V. Nicolosi, M. Lotya, F. M. Blighe, Z. Sun, S. De, I. McGovern, B. Holland, M. Byrne, Y. K. Gun'Ko, *et al.*, *Nat. Nanotechnol.*, 2008, **3**, 563.
68 F. Bonaccorso, A. Lombardo, T. Hasan, Z. Sun, L. Colombo and A. C. Ferrari, *Mater. Today*, 2012, **15**, 564.
69 M. Lotya, P. J. King, U. Khan, S. De and J. N. Coleman, *ACS Nano*, 2010, **4**, 3155.
70 A. C. Ferrari, F. Bonaccorso, V. Fal'ko, K. S. Novoselov, S. Roche, P. Boggild, S. Borini, F. H. L. Koppens, V. Palermo, N. Pugno, *et al.*, *Nanoscale*, 2015, **7**, 4598.
71 S. C. Anenberg, J. Miller, R. Minjares, L. Du, D. K. Henze, F. Lacey, C. S. Malley, L. Emberson, V. Franco, Z. Klimont and C. Heyes, *Nature*, 2017, **545**, 467.
72 J. Lelieveld, J. S. Evans, M. Fnais, D. Giannadaki and A. Pozzer, *Nature*, 2015, **525**, 367.
73 Á. Tolosana-Moranchel, A. Manassero, M. L. Satuf, O. M. Alfano, J. A. Casas and A. Bahamonde, *Appl. Catal., B*, 2019, **246**, 1.
74 Y. Huang, D. Chen, X. Hu, Y. Qian and D. Li, *Nanomaterials*, 2018, **8**, 431.
75 N. Kobayashi, H. Izumi and Y. Morimoto, *J. Occup. Health*, 2017, **59**, 394.
76 C. Martín, K. Kostarelos, M. Prato and A. Bianco, *Chem. Commun.*, 2019, **55**, 5540.
77 S. Gurunathan and J.-H. Kim, *Int. J. Nanomed.*, 2016, **11**, 1927.
78 D. M. Mitrano, S. Motellier, S. Clavaguera and B. Nowack, *Environ Int*, 2015, **77**, 132.
79 J. Luo, S. Zhang, M. Sun, L. Yang, S. Luo and J. C. Crittenden, *ACS Nano*, 2019, **13**, 9811–9840.
80 K. Wenderich and G. Mul, *Chem. Rev.*, 2016, **116**, 14587.
81 J. Jiang, X. He, J. Du, X. Pang, H. Yang and Z. Wei, *Mater. Lett.*, 2019, **244**, 178.
82 A. Tayel, R. A. Ramadan and A. O. El Seoud, *Catalysts*, 2018, **8**, 491.
83 Á. Tolosana-Moranchel, A. Casasa, A. Bahamonde, L. Pascual, L. I. Granone, J. Schneider, R. Dillert and D. W. Bahnemann, *Appl. Catal., B*, 2019, **241**, 375.
84 G. Luna-Sanguino, Á. Tolosana-Moranchel, C. Duran-Valle, M. Faraldos and A. Bahamonde, *Catal. Today*, 2019, **328**, 172.
85 http://www.42teknanomaterials.com/.
86 http://www.northerngraphite.com/.
87 R. A. Young, *The Rietveld method*, International union of crystallography, 1993.

88 O. Tanaike and M. Inagaki, *Carbon*, 1997, **35**, 831.
89 A. N. Fitch, *J. Res. Natl. Inst. Stand. Technol.*, 2004, **109**, 133.
90 W. Li, R. Liang, A. Hu, Z. Huang and Y. N. Zhou, *RSC Adv.*, 2014, **4**, 36959.
91 B. H. Toby, *J. Appl. Crystallogr.*, 2001, **34**, 210.
92 C. E. Holcombe, *Report Y 1887*, USAEC Oak Ridge Y 12 Plant, 1973.
93 B. H. Toby and R. B. Von Dreele, *J. Appl. Crystallogr.*, 2013, **46**, 544.
94 P. Kubelka and F. Munk, *Z. Tech. Phys.*, 1931, **12**, 593.
95 G. Kortüm, *Reflectance spectroscopy: principles, methods, applications*, Springer Science & Business Media, 2012.
96 J. Workman Jr. and A. Springsteen, *Applied spectroscopy: a compact reference for practitioners*, Academic Press, 1998.
97 A. A. Christy, O. M. Kvalheim and R. A. Velapoldi, *Vib. Spectrosc.*, 1995, **9**, 19.
98 S. D. Jackson and J. S. J. Hargreaves, *Metal Oxide Catalysis*, John Wiley & Sons, 2009.
99 K. M. Reddy, S. V. Manorama and A. R. Reddy, *Mater. Chem. Phys.*, 2003, **78**, 239.
100 A. Murphy, *Sol. Energy Mater. Sol. Cells*, 2007, **91**, 1326.
101 T. Smausz, B. Kondász, T. Gera, T. Ajtai, N. Utry, M. D. Pintér, G. Kiss-Albert, J. Budai, Z. Bozóki, G. Szabo, *et al.*, *Appl. Phys. A*, 2017, **123**, 633.
102 S. Ngamta, N. Boonprakob, N. Wetchakun, K. Ounnunkad, S. Phanichphant and B. Inceesungvorn, *Mater. Lett.*, 2013, **105**, 76.
103 R. Jain, M. Mathur, S. Sikarwar and A. Mittal, *J. Environ. Manage.*, 2007, **85**, 956.
104 G. Guidetti, A. Cantelli, R. Mazzaro, L. Ortolani, V. Morandi and M. Montalti, *Nanoscale*, 2016, **8**, 8505.
105 S. P. Patil, B. Bethi, G. H. Sonawane, V. S. Shrivastava and S. Sonawane, *J. Ind. Eng. Chem.*, 2016, **34**, 356.
106 T. S. Natarajan, M. Thomas, K. Natarajan, H. C. Bajaj and R. J. Tayade, *Chem. Eng. J.*, 2011, **169**, 126.
107 P. Zhu, A. S. Nair, S. Peng, S. Yang and S. Ramakrishna, *ACS Appl. Mater. Interfaces*, 2012, **4**, 581.
108 F. Zhou, C. Yan, T. Liang, Q. Sun and H. Wang, *Chem. Eng. Sci.*, 2018, **183**, 231.
109 K. Rajeshwar, M. Osugi, W. Chanmanee, C. Chenthamarakshan, M. Zanoni, P. Kajitvichyanukul and R. Krishnan-Ayer, *J. Photochem. Photobiol., C*, 2008, **9**, 171.
110 http://www.fotocatalisis.org/assets/doc497.pdf.
111 R. Zouzelka and J. Rathousky, *Appl. Catal., B*, 2017, **217**, 466.
112 http://www.fei.com/products/vitrobot.
113 H. Friedrich, P. M. Frederik, G. de With and N. A. Sommerdijk, *Angew. Chem., Int. Ed.*, 2010, **49**, 7850.
114 T. Ohsaka, F. Izumi and Y. Fujiki, *J. Raman Spectrosc.*, 1978, **7**, 321.
115 P. A. Temple and C. E. Hathaway, *Phys. Rev. B*, 1973, **7**, 3685.
116 V. Swamy, A. Kuznetsov, L. S. Dubrovinsky, R. A. Caruso, D. G. Shchukin and B. C. Muddle, *Phys. Rev. B*, 2005, **71**, 184302.
117 A. C. Ferrari, *et al.*, *Phys. Rev. Lett.*, 2006, **97**, 187401.
118 A. C. Ferrari and J. Robertson, *Phys. Rev. B*, 2000, **61**, 14095.
119 F. Tuinstra and J. L. Koenig, *J. Chem. Phys.*, 1970, **53**, 1126.
120 M. Bruna, A. K. Ott, M. Ijaes, D. Yoon, U. Sassi and A. C. Ferrari, *ACS Nano*, 2014, **8**, 74327441.
121 L. G. Cancado, A. Jorio, E. H. Martins Ferreira, F. Stavale, C. A. Achete, R. B. Capaz, M. V. O. Moutinho, A. Lombardo, T. S. Kulmala and A. C. Ferrari, *Nano Lett.*, 2011, **11**, 3190.
122 D. E. Gu, Y. Lu and B. C. Yang, *Chem. Commun.*, 2008, **21**, 2453.
123 T. Takizawa, T. Watanabe and K. Honda, *J. Phys. Chem.*, 1978, **82**, 1391.
124 S. H. Szczepankiewicz, J. A. Moss and M. R. Hoffmann, *J. Phys. Chem. B*, 2002, **106**, 2922.
125 T. Yoshihara, R. Katoh, A. Furube, Y. Tamaki, M. Murai, K. Hara, S. Murata, H. Arakawa and M. Tachiya, *J. Phys. Chem. B*, 2004, **108**, 3817.
126 A. Yamakata, T. A. Ishibashi and H. Onishi, *Chem. Phys. Lett.*, 2001, **333**, 271.
127 A. Yamakata, T. A. Ishibashi and H. Onishi, *J. Phys. Chem. B*, 2001, **105**, 7258.
128 F. J. Knorr, C. C. Mercado and J. L. McHale, *J. Phys. Chem. C*, 2008, **112**, 12786.
129 J. Schneider, M. Matsuoka, M. Takeuchi, J. Zhang, Y. Horiuchi, M. Anpo and D. W. Bahnemann, *Chem. Rev.*, 2014, **114**, 9919.
130 Y. Tamaki, A. Furube, R. Katoh, M. Murai, K. Hara, H. Arakawa and M. Tachiya, *C. R. Chim.*, 2006, **9**, 268.
131 M. Breusing, S. Kuehn, T. Winzer, E. Malic, F. Milde, N. Severin, J. P. Rabe, C. Ropers, A. Knorr and T. Elsaesser, *Phys. Rev. B*, 2011, **83**, 153410.
132 D. Sun, Z. K. Wu, C. Divin, X. Li, C. Berger, W. A. de Heer, P. N. First and T. B. Norris, *Phys. Rev. Lett.*, 2008, **101**, 157402.
133 D. Brida, A. Tomadin, C. Manzoni, Y. J. Kim, A. Lombardo, S. Milana, R. R. Nair, K. S. Novoselov, A. C. Ferrari, G. Cerullo and M. Polini, *Nat. Commun.*, 2013, **4**, 1987.
134 A. Tomadin, D. Brida, G. Cerullo, A. C. Ferrari and M. Polini, *Phys. Rev. B*, 2013, **88**, 035430.
135 K. Iwata, T. Takaya, H. O. Hamaguchi, A. Yamakata, T. A. Ishibashi, H. Onishi and H. Kuroda, *J. Phys. Chem. B*, 2004, **108**, 20233.
136 Y. Tamaki, A. Furube, M. Murai, K. Hara, R. Katoh and M. Tachiya, *Phys. Chem. Chem. Phys.*, 2007, **9**, 1453.
137 A. Furube, T. Asahi, H. Masuhara, H. Yamashita and M. Anpo, *Chem. Phys. Lett.*, 2001, **336**, 424.

